Tenth International Conference on Computational Fluid Dynamics (ICCFD10), Barcelona, Spain, July 9-13, 2018

ICCFD10-2018-156

Large-eddy simulation of controlled and uncontrolled turbulent boundary layers

P.D. Boom*, S. Rolston** and D.W. Zingg*
Corresponding author: pieter.boom@mail.utoronto.ca

* University of Toronto Institute for Aerospace Studies, Canada.
** Airbus Group Innovations, United Kingdom.

Abstract: This article presents a comparison of the implicit (no model) large-eddy simulation (LES) technique and the local integral length-scale approximation (ILSA) subfilter model. The focus is on the numerical simulation of flat plate turbulent boundary layers and active flow control using synthetic jets. After initial verification of the simulation setup, comparative studies are presented to investigate the dependence on spatial and temporal resolution, the level of artificial dissipation, and some additional simulation parameters. Overall the ILSA model produces slightly more consistent and accurate results than the implicit LES approach. It also reduces computational cost by reducing the number of linear iterations required at each stage of the time-marching method. The controlled results generated by the implicit LES are in reasonably good agreement with experiment and give additional details of the spatial change in time-average skin friction. However, more work is needed to efficiently apply the ILSA model to the controlled case. Instabilities originating in the slot of the jet limited the ILSA model to a time step size one to two orders of magnitude smaller than the implicit LES approach.

Keywords: Large-Eddy Simulation, Integral Length-Scale Approximation Model, High-Order Methods, Turbulent Boundary Layers, Flow Control, Synthetic Jets

1 Introduction

Fuel has become one of the dominant operating costs for commercial airlines [1]. Furthermore, the burning of fossil fuels has a negative impact on both local air quality and global climate change [2, 3, 4]. The amount of fuel burned by aircraft is directly related to their drag. For a typical commercial aircraft, over 50% of total aircraft drag is due to viscous drag. The skin friction caused by the interaction of the turbulent boundary layer with the aircraft surface is the key contributor to this drag term. Active turbulent boundary layer control is one promising approach to reducing skin friction drag and thus fuel burn.

Numerical simulation can play a significant role in the development of new flow control technologies. It provides a complete description of the entire flow field, including derived quantities such as vorticity or the Q-criterion. This can help identify different structures in the flow and the influence of the control strategy on those structures. Furthermore, it can be used to relate the influence of the control to experimentally observable quantities, such as wall pressure or skin-friction, to better develop closed loop control strategies for practical application. Other benefits of numerical simulation include the ability to have complete control over simulation and boundary conditions, to integrate numerical optimization for sensor or actuator placement, and the ease of geometry manipulation.

While direct numerical simulation (DNS) of the turbulent boundary layer and control mechanisms would be ideal, it is also prohibitively expensive. For studies of larger parameter sets or higher Reynolds numbers, large-eddy simulation (LES) is an attractive alternative. With this approach the aim is to simulate the large energetic scales in the flow, while applying a model for the small and mostly dissipative scales. Modern actuators do not have the temporal or spatial response required to manipulate the smaller structures in wall bounded turbulent flows; however, Hutchins and Marusic [5] found evidence of large superstructures in the logarithmic region of the boundary layer. These superstructures correlate to turbulent activity near the wall [6]. This phenomenon becomes increasingly significant with Reynolds number. The simulation of control strategies targeted at large structures formed at higher Reynolds numbers align well with the capabilities of the LES approach.

One common LES approach is to under resolve a direct numerical simulation without adding a model for the subgrid scales. This is called the implicit LES technique. The numerical methods used to stabilize the governing equations, for example numerical filtering or artificial dissipation, function as a subgrid model for the smallest scales in the flow. This can also be viewed as solving the Favre-filter Navier-Stokes equations with zero turbulent-eddy viscosity (no model LES). Despite little physical motivation for the way in which the subgrid scales are handled, it has been successfully applied a range of turbulent flow fields, including wall bounded flows [7, 8, 9]. This approach is inexpensive, with minimum implementation and computational cost.

Another approach is to include a physically motivated subgrid model. One such model is the local Integral Length-Scale Approximation (ILSA) model developed by Rouhi *et al.* [10]. This is an algebraic eddy-viscosity model which seeks to generate a grid-independent approximation of the integral length scale. For this reason, it has been described as a subfilter model, rather than subgrid model. The ILSA model uses a spatially and temporally varying model constant to enforce a prescribed level of subfilter activity locally, which is a particular benefit for wall bounded flows [10]. The ILSA model does not require the solution to additional transport equations, making it a relatively low cost upgrade to the implicit LES approach.

This paper presents a comparison of the two LES techniques discussed above. The focus is on their relative performance for simulating flat plate turbulent boundary layers and active flow control using a spanwise oriented synthetic jet. The models' behaviour at various spatial and temporal resolutions, along with different simulation parameters, is investigated. An assessment of their suitability for controlled simulations with reference to experimental data is also be presented.

Section 2 presents a brief description of the flow solver used in this work, the governing equations, and the two large-eddy simulation techniques considered. This is followed by a description of the computational domain, boundary conditions, and grids in Section 3. An initial low-Reynolds number uncontrolled simulation is presented in Section 4, followed by a comparison of the two models applied to a higher-Reynolds number set of simulations in Section 5. The performance of the methods applied to a controlled simulation using a single synthetic jet is discussed in Section 6. Section 7 summaries the conclusions of this work.

2 Flow Solver and Subfilter Model

Numerical simulations are carried out using the three-dimensional compressible flow solver called DIABLO, which can solve either the Naver-Stokes or Favre filtered Navier-Stokes equations. The spatial discretization is obtained using fourth-order finite-difference summation-by-parts (SBP) operators on C^0 continuous structured multiblock grids. Boundary conditions and block interface coupling are weakly enforced with simultaneous approximation terms (SATs). The discretization is stabilized with high-order matrix artificial dissipation compatible with the SBP-SAT approach. Temporal integration is obtained with fourth-order explicit-first-stage singly-diagonally-implicit Runge-Kutta (ESDIRK4) methods [11]. Additional details of the flow solver can be found in the following references [12, 13, 14, 15, 16].

2.1 Favre Filtered Navier-Stokes Equations

The non-dimensional Favre filtered Navier-Stokes equations in curvilinear coordinates are written as

$$\frac{\partial Q}{\partial t} + \frac{\partial E_i}{\partial \xi_i} = \frac{1}{Re}\left[\frac{\partial E_{v,i}}{\partial \xi_i}\right], \tag{1}$$

where Re is the Reynolds number. The vector of conserved variables is

$$Q = \mathcal{J}^{-1}\left[\overline{\rho},\ \overline{\rho}\widetilde{u}_1,\ \overline{\rho}\widetilde{u}_2,\ \overline{\rho}\widetilde{u}_3,\ \overline{\rho}\widetilde{e}\right]^T, \tag{2}$$

where $\mathcal{J}$ is the metric Jacobian of the curvilinear coordinate transformation, $\overline{\rho}$ is the density, $\widetilde{u}_i$ are the Cartesian velocity components, and $\widetilde{e}$ is the total energy per unit mass. The flow variables ($\overline{\rho}$, $\widetilde{u}_i$, $\widetilde{e}$) represent the resolved low-frequency components of a density-weighted Favre filtering process

$$\phi = \underbrace{\widetilde{\phi}}_{\text{resolved}} + \underbrace{\phi''}_{\text{subfilter}}, \tag{3}$$

where

$$\widetilde{\phi} = \frac{\overline{\rho\phi}}{\overline{\rho}}, \tag{4}$$

and $\overline{\phi}$ is the Reynolds average.

The governing equations (1) are non-dimensionalized using the following relationships

$$t = \frac{\hat{t}\,\hat{a}_\infty}{\hat{c}}, \quad x_i = \frac{\hat{x}_i}{\hat{c}}, \quad \rho = \frac{\hat{\rho}}{\hat{\rho}_\infty}, \quad u_i = \frac{\hat{u}_i}{\hat{a}_\infty}, \quad e = \frac{\hat{e}}{\hat{\rho}_\infty^2 \hat{a}_\infty^2}, \quad \mu = \frac{\hat{\mu}}{\hat{\mu}_\infty}, \tag{5}$$

where $\hat{\phi}$ denotes a dimensional quantity, and the subscript ∞ denotes a free-stream value. The characteristic length scale is denoted $\hat{c}$, and $a = \sqrt{\gamma p/\rho}$ is the speed of sound, where p is the pressure and $\gamma = 1.4$ is the specific heat ratio. The Reynolds number in (1) is thus defined as $Re = \frac{\hat{\rho}_\infty \hat{a}_\infty \hat{c}}{\hat{\mu}_\infty}$, for the freestream molecular viscosity $\hat{\mu}_\infty$. The inviscid and viscous fluxes in (1) are

$$E_i = \begin{bmatrix} \overline{\rho}\widetilde{u}_i \\ \overline{\rho}\widetilde{u}\widetilde{U}_i + \xi_{i,x_1}\overline{p} \\ \overline{\rho}\widetilde{u}\widetilde{U}_i + \xi_{i,x_2}\overline{p} \\ \overline{\rho}\widetilde{u}\widetilde{U}_i + \xi_{i,x_3}\overline{p} \\ (\overline{\rho}\widetilde{e} + \overline{p})\widetilde{U}_i \end{bmatrix}, \quad \text{and} \quad E_{v,i} = \begin{bmatrix} 0 \\ \widetilde{\tau}_{x_i x_1} \\ \widetilde{\tau}_{x_i x_2} \\ \widetilde{\tau}_{x_i x_3} \\ \widetilde{u}_j \widetilde{\tau}_{x_i x_j} + \frac{\mu Pr^{-1} + \mu_t Pr_t^{-1}}{\gamma - 1} \xi_{j,x_i} \overline{a}^2_{\xi_j} \end{bmatrix}, \tag{6}$$

respectively, where $\widetilde{U}_i = \xi_{i,x_j}\widetilde{u}_j$ are the contravariant velocities, and $Pr = 0.72$ and $Pr_t = 0.9$ are the laminar and turbulent Prandtl numbers, respectively. The components of the stress tensor are defined as

$$\widetilde{\tau}_{x_i x_j} = 2(\mu + \mu_t)\widetilde{S}^*_{ij}, \tag{7}$$

where μ_t is the turbulent eddy viscosity discussed in the following sections, $\widetilde{S}^*_{ij} = \widetilde{S}_{ij} - \frac{1}{3}\delta_{ij}\widetilde{S}_{kk}$ is the deviatoric strain-rate tensor, $\widetilde{S}_{ij} = \frac{1}{2}\left(\xi_{k,x_i}\widetilde{u}_{j,\xi_k} + \xi_{k,x_j}\widetilde{u}_{i,\xi_k}\right)$ is the standard strain-rate tensor, and δ_{ij} is the Kronecker delta. The equation of state is $\overline{p} = \overline{\rho}(\gamma - 1)\left(\widetilde{e} - \frac{1}{2}\left(\widetilde{u}_i^2\right)\right)$ and the non-dimensional molecular viscosity is calculated using Sutherland's law

$$\mu = \frac{\overline{a}^3(1 + \mathcal{S}/T_\infty)}{\overline{a}^2 + \mathcal{S}/T_\infty}, \tag{8}$$

where $\overline{a} = \sqrt{\gamma\overline{p}/\overline{\rho}}$, $\mathcal{S} = 198.6^\circ R$ is Sutherland's constant, and $T_\infty = 460^\circ R$ is the free-stream temperature.

In the derivation of the governing equations (1) we have applied the eddy-viscosity approximation

$$-\overline{\rho u_i'' u_j''} = \widetilde{\tau}^a_{t,ij} = \widetilde{\tau}_{t,ij} - \frac{\delta_{ij}}{3}\widetilde{\tau}_{t,kk} = -2\mu_t \widetilde{S}^*_{ij}. \tag{9}$$

We have also used Fourier's law $q_i = \frac{\mu}{Pr(\gamma-1)}\xi_{j,x_i}\overline{a}^2_{\xi_j}$ and assumed that $C_p\overline{\rho u_j'' T} = \frac{\mu_t}{Pr_t(\gamma-1)}\xi_{j,x_i}\overline{a}^2_{\xi_j}$, where C_p is the specific heat capacity under constant pressure. In contrast, we have assumed that $C_p\frac{\mu}{Pr}\xi_{j,x_i}\overline{T''}_{\xi_j}$ is negligible. We have assumed that $|\overline{\tau''}_{ij}| << |\widetilde{\tau}_{ij}|$ and therefore terms with $\overline{\tau''}_{ij}$ are neglected. Likewise, we have assumed that the turbulent kinetic energy is small compared to the enthalpy and therefore we have neglected terms $\frac{1}{2}\overline{\rho u_j'' u_i'' u_i''}$ and $\overline{u_i''\tau_{ij}}$. Finally, we have neglected fluctuations in the molecular viscosity.

To simplify the presentation in the remainder of this article we will drop the diacritics associated with the Favre averaging. As an example, it will be assumed $Q = \mathcal{J}^{-1}[\rho,\, \rho u_1,\, \rho u_2,\, \rho u_3,\, \rho e]^T$ represents only the resolved flow variables.

2.2 Implicit Large-Eddy Simulation

In implicit large-eddy simulation the contribution from the subfilter scales (ϕ'') is assumed to be modelled implicitly by the numerical stabilization of the discretized governing equations. This implies that the turbulent eddy viscosity in the viscous fluxes of (1) is zero. While there is less physical motivation for this approach, it is: 1) easy to implement, 2) relatively inexpensive computationally, and 3) has been shown to generate accurate results for wall-bounded turbulent flows [7, 8, 9]. In the present approach, the stabilization is provided by a matrix artificial dissipation model.

2.3 Integral Length Scale Approximation Model

The integral length scale approximation model (ILSA) is an algebraic eddy-viscosity model. It seeks to model the influence of the subfilter scales through a turbulent eddy viscosity

$$\mu_t = \rho (C_k L_{\mathrm{est}})^2 ||S||, \tag{10}$$

where the norm is computed $||S|| = \sqrt{2 S_{ij} S_{ij}}$, and C_k is a model coefficient. A primary goal in the development of the ILSA model was to obtain an approximation of the integral length scale which becomes grid independent beyond a certain level of grid refinement [10]. The approximation used is

$$L_{\mathrm{est}} = \frac{< \mathcal{K}_{\mathrm{res}} >^{3/2}}{< \epsilon_{\mathrm{tot}} >}, \tag{11}$$

where $< \phi >$ denotes an average over one or more homogeneous directions in the flow. In this work we use a time-averaging of the form

$$< \phi^{[n+1]} > = \left(1 - \frac{dt}{T_{\mathrm{avg}}}\right) < \phi^{[n]} > + \frac{dt}{T_{\mathrm{avg}}} \phi^{[n]}, \tag{12}$$

where T_{avg} is the averaging time scale. The turbulent kinetic energy of the resolved field is $\mathcal{K}_{\mathrm{res}} = \frac{1}{2} u'_i u'_i$, where the fluctuating values are computed as $\phi' = \phi - < \phi >$. The turbulent dissipation rate of the resolved and subfilter fields is computed using

$$\begin{aligned} \rho \epsilon_{\mathrm{res}} &= 2 \mu S'^{*}_{ij} \xi_{k,x_i} u_{j,\xi_k} = 2 \mu S'^{*}_{ij} S'^{*}_{ij} = \mu ||S'^{*}||^2, \\ \rho \epsilon_{\mathrm{flt}} &= 2 \mu_t S'^{*}_{ij} \xi_{k,x_i} u_{j,\xi_k} = 2 \mu_t S'^{*}_{ij} S'^{*}_{ij} = \mu_t ||S'^{*}||^2, \\ \rho \epsilon_{\mathrm{tot}} &= (\mu + \mu_t) \, ||S'^{*}||^2. \end{aligned} \tag{13}$$

Combining these definitions, we see that the turbulent eddy viscosity is defined implicitly via

$$\mu_t = \rho \left(C_k \frac{< \frac{1}{2} u'_i u'_i >^{3/2}}{< \frac{(\mu + \mu_t)}{\rho} ||S'^{*}||^2 >} \right)^2 ||S||. \tag{14}$$

Following Rouhi *et al.* [10], we evaluate the averaged quantities at the previous time step to make the expression explicit.

A key aspect of the model is the definition of the division between resolved and subfilter scales, which is accomplished through the spatially and temporally varying model coefficient. The model coefficient is based on an approximation of the subfilter activity

$$s_\tau = \left[\frac{< \tau^a_{t,ij} \tau^a_{t,ij} >}{< (\tau^a_{t,ij} + R^a_{ij})(\tau^a_{t,ij} + R^a_{ij}) >} \right]^{1/2} \tag{15}$$

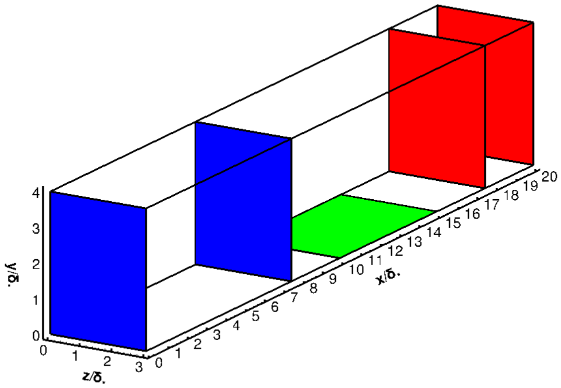

Figure 1: Computational domain and boundary conditions. Blue planes denote inflow and recycle planes. Red planes denote the convective outflow plane and the reference plane. The green region denotes the working region.

where

$$R^a_{ij} = u'_i u'_j - \frac{\delta_{ij}}{3} u'_k u'_k, \tag{16}$$

is the anisotropic part of the resolved stresses. Substituting the eddy-viscosity approximation and the ILSA eddy viscosity, we obtain a quadratic equation for the square of the model coefficient

$$\chi_1 \left(1 - (1/s_\tau)^2\right) C_k^4 - \chi_2 C_k^2 + \chi_3 = 0, \tag{17}$$

where

$$\begin{aligned} \chi_1 &=< 2L_{est}^4 ||S||^2 ||S^*||^2 >, \\ \chi_2 &=< 4L_{est}^2 ||S|| S^*_{ij} R^a_{ij} >, \\ \chi_3 &=< R^a_{ij} R^a_{ij} >=< \tfrac{8}{3} \mathcal{K}^2_{res} >, \end{aligned} \tag{18}$$

and the averaging is computed over homogeneous directions in the flow. Again, in the present work we average in time only, and averaged quantities are evaluated at the end of the previous time step.

2.3.1 Linearization of the turbulent eddy viscosity

The preconditioner used in the implicit Newton-Krylov-Schur solution process requires a linearization of the turbulent eddy viscosity. This is computed for the local ILSA model as follows

$$\frac{\partial \mu_t}{\partial Q} = \begin{bmatrix} 2(C_k L_{est})^2 \xi_{i,x_j} \rho_{\xi_i} (u_k S_{ik}) \\ -2(C_k L_{est})^2 \xi_{i,x_j} \rho_{\xi_i} S_{i1} \\ -2(C_k L_{est})^2 \xi_{i,x_j} \rho_{\xi_i} S_{i2} \\ -2(C_k L_{est})^2 \xi_{i,x_j} \rho_{\xi_i} S_{i3} \\ 0 \end{bmatrix}^T . \tag{19}$$

3 Simulation Setup: Domain, Grid, and Boundary Conditions

The computational domain is constructed relative to a target 99% boundary-layer thickness $\delta_\circ$. This also defines the characteristic length $\hat{c}$ used in the non-dimensionalization of the governing equations. Using this reference length scale, the size of the domain used for the initial uncontrolled simulation and in the controlled case is $(20 \times 4 \times 3)\delta_\circ$ in the streamwise, wall-normal, and spanwise directions, respectively. The working region where data is collected and analysed is $x \in [10, 15]\delta_\circ$. Figure 1 shows a schematic of the domain. The size and location of the working region is chosen to minimize the influence of the artificial inflow and outflow boundary conditions on the data collected. Likewise, the spanwise dimension is chosen to ensure that spanwise periodicity does not influence the turbulent flow field and to minimize the interaction of the synthetic jet across the periodic boundaries. For the comparison studies, a smaller domain spanning $(10 \times 3 \times 3)\delta_\circ$ is used to minimize computational cost. Data is collected from the plane located at $7.5\delta_\circ$ from the inlet.

The flat plate is simulated with a no-slip adiabatic wall boundary condition using a high-order SBP approximation of the temperature gradient. To avoid simulating the entire synthetic jet (slot, cavity, and diaphragm), a velocity boundary condition is imposed at the base of the slot to model the diaphragm and cavity. The velocity profile is sinusoidal in time and trapezoidal in space with the prescribe velocity covering 78.8% of the slot base and decaying to zero at the walls of the slot. The turbulent inflow data is generated using the recycle/rescale approach proposed by Lund *et al* [17] and the compressible extension for density and temperature presented in Stolz and Adams [18]. Based on the target Re_θ, empirical relationships are used to determine the simulation Reynolds number $Re_{\delta_\circ}$ and the inlet boundary-layer thickness for the rescaling procedure. The recycle plane is located at $x = 6.25\delta_\circ$ and $7.5\delta_\circ$ in the smaller and larger simulation domains, respectively. These locations are chosen to minimize errors introduced by the recycling procedure itself and disturbances created by the synthetic jets located at $x = 10\delta_\circ$. A convective boundary condition is imposed at the outflow (see for example [19]):

$$\frac{\partial Q}{\partial t} + < u > \frac{\partial Q}{\partial x}\bigg|_{\text{outflow}} = 0, \tag{20}$$

where Q is the vector of conserved flow variables, and $< u >$ is the convection velocity obtained from the mean flow $1.25\delta_\circ$ and $2.5\delta_\circ$ upstream of the boundary for the smaller and larger simulation domains, respectively. This is done to decouple the outflow condition from the solution at the boundary itself, mitigating potential instabilities. The assumption is that the mean boundary-layer properties do not vary significantly between the reference and boundary planes. At the top of the domain, a characteristic boundary condition is applied in the uncontrolled simulations and the solution is extrapolated from the interior for the controlled. Finally, as alluded to above, the spanwise walls of the computational domain are periodic.

The computational domain is discretized into orthogonal structured multiblock grids. The grids are equally spaced in the streamwise and spanwise directions, and have hyperbolic tangent spacing in the wall-normal direction. They are decomposed into blocks of $33 \times 33 \times 16$ or 33^3 nodes, depending on the simulation, and the solution is computed in parallel. Table 1 presents the details regarding mesh spacing and node counts. In the controlled case, the grid is refined in the vicinity of the synthetic jet. Furthermore, an additional block is added for the slot itself. The slot in the present simulation has dimensions $0.3\delta_\circ$ wide, $\sim 0.023\delta_\circ$ long, and $0.075\delta_\circ$ deep. The resulting block topology for the controlled simulation domain is shown in Figure 2. The block topology and grid distribution near the jet is shown in Figure 3.

4 Low Reynolds Number Uncontrolled Simulations

Before comparing the two LES approaches, we verify that our flow solver can replicate the desired zero pressure gradient flat plate boundary layer. This is done with the implicit LES approach. The flow solver applied in this work is compressible, therefore a Mach number of 0.2 is chosen to ensure that the numerical solution is well-conditioned without the use of low Mach number preconditioning. This is high relative to many low speed experimental data sets we use for comparison, but the impact is expected to be negligible. The selection of a lower target momentum thickness Reynolds number $Re_\theta = 1500$ is done to generate a relatively well resolved flow field, while minimizing computational cost. With the end goal of simulating synthetic jets for flow control, the larger simulation domain is selected. The results presented below are obtained using a time step of $\Delta t = 0.04$ in non-dimensional time units.

In this simulation, the Re_θ realized at the beginning of the working region is just over 1600, slightly higher than the target value set at $Re_\theta = 1500$. The Re_τ realized at the same location is over 650, the shape

Simulation	Nodes				Spacing		
	N_x	N_y	N_z	N_{tot}	x^+_{max}	y^+_{min}	z^+_{max}
Uncontrolled - $Re_\theta = 1500$							
Baseline	961	129	289	$\sim 39 \times 10^6$	13	0.5	6.5
Uncontrolled - $Re_\theta = 3230$							
Coarse	121	129	225	$\sim 4 \times 10^6$	94	0.9	15
Medium -Baseline	241	161	321	$\sim 14 \times 10^6$	47	0.5	11
Fine	481	193	449	$\sim 47 \times 10^6$	23	0.5	7.5
streamwise	481	161	321	$\sim 28 \times 10^6$	23	0.5	11
spanwise	241	161	449	$\sim 20 \times 10^6$	47	0.5	7.5
wall-normal	241	225	321	$\sim 20 \times 10^6$	47	0.5	11
Controlled - $Re_\theta = 4210$							
Baseline	545	161	289	$\sim 27 \times 10^6$	54	1	14
-slot(x1)	13	65	33	$\sim 2.8 \times 10^4$	2	1	13

Table 1: Grid details for the uncontrolled and controlled simulations. Note that the number of nodes given in each direction is the number of unique computational nodes in that direction, whereas the approximate total number of nodes given includes repeated nodes at block interfaces.

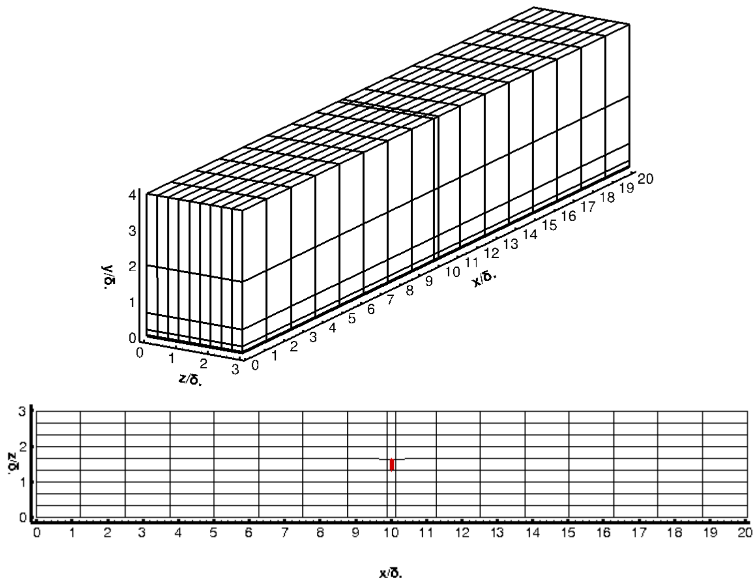

Figure 2: Block topology for controlled simulations.

factor is about 1.45, and the friction velocity scaled by the freestream flow velocity is 0.0017.

Figure 4a shows the mean streamwise velocity profile, along with the empirical curves for the viscous sublayer and law of the wall. Compared with theory, the velocity in the present simulation is slightly overpredicted in the buffer layer, which then extends through the log region. The slope in the log layer is, however, reasonably well predicted. This behaviour is observed in many other LES simulations [20, 21, 22]. Sayadi and Moin [20], who compared several different LES approaches to DNS results, were able to improve the agreement of the LES models in the buffer layer only by significantly increasing the grid resolution. The results of the present implicit LES simulation lie very close to these fine grid results from Sayadi and Moin, when overlaid with each other (not shown here).

Consider the streamwise velocity fluctuations shown in Figure 4b. The present simulation over predicts the magnitude of the peak fluctuations as compared to the DNS results from Wu and Moin [23] at $Re_\theta = 900$. The present peak value is 3, as compared to 2.75 in the reference. This behaviour continues through the

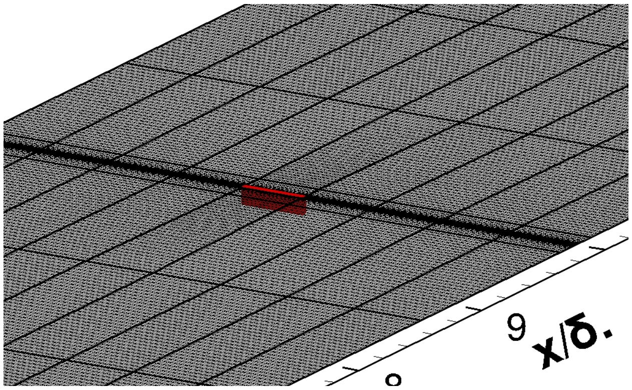

Figure 3: Block topology and grid near a synthetic jet, with the additional block needed to simulate the slots shown in red.

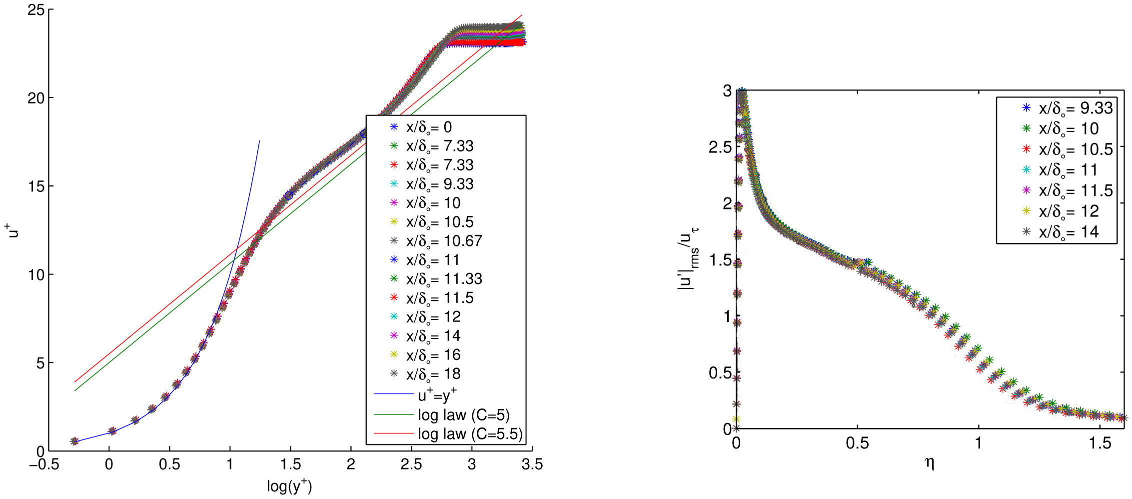

(a) Streamwise mean velocity profiles.

(b) Streamwise fluctuation velocity profiles.

Figure 4: **Implicit LES -** $Re_\theta = 1500$**.**

logarithmic region, similar to the mean velocity profiles discussed above. Note that the Reynolds number in the reference simulation is lower; however, this does not account for all of the deviation. Again, these deviations are consistent with the use of LES.

Diagnostic plots show empirical relations for the streamwise velocity fluctuations as a function of the mean velocity profile [25]. Figure 5a highlights the observed linear region in the outer part of the boundary layer superimposed on the linear fit presented in Alfredsson et al. [24]. The fluctuations exhibit the correct slope, but are a little over predicted. Figure 5b highlights the linear region observed near the wall superimposed on the linear fit presented in Alfredsson et al. [25] (Note the different axes). The present simulations match well with the linear fit.

The results presented above match reasonably well with the reference theory and simulations. The observed deviations are consistent with the use of LES modelling observed in the literature. To eliminate other possible sources of error which can cause a shift in velocity profiles, we also investigate compressibility effects and the strength of any pressure gradients in the present simulations.

Compressibility can have a significant impact on the expected boundary-layer profiles, causing a shift in the law of the wall (see for example [26]). This is primarily a concern with supersonic boundary layers, but can influence subsonic flows as well (for example [27, 28]). The present simulations are performed at a higher Mach number than the reference experiments, $M = 0.2$, but within the incompressible regime and

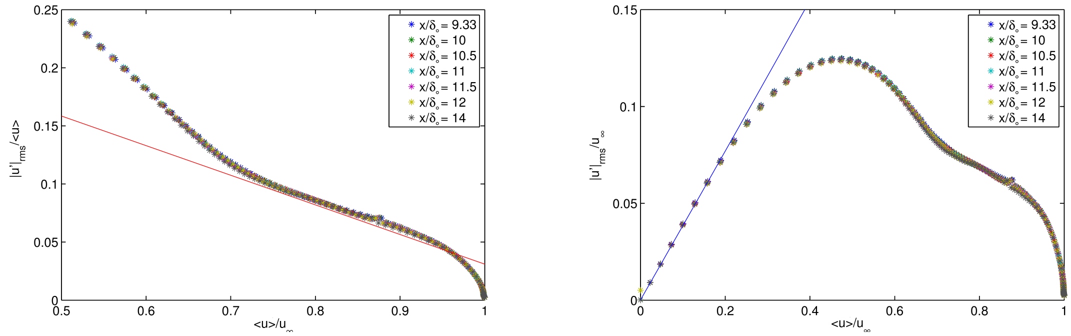

(a) Streamwise velocity fluctuation profiles with linear fit from Alfredsson *et al.* [24].

(b) Streamwise velocity fluctuation profiles with linear fit from Alfredsson *et al.* [25].

Figure 5: **Implicit LES -** $Re_\theta = 1500$**.**

hence the influence of compressibility is expected to be negligible. Indeed the density and temperature vary by less than 2% throughout the whole domain. As further verification, the van Driest transformed log-law velocity profile [29] is computed. Comparing the transformed and untransformed profiles yields a difference on the order of 1%. This supports the assumption that compressibility effects are negligible in the present simulations.

Favourable and adverse pressure gradients can also have a significant impact on the resulting boundary-layer properties. To ensure that little or no pressure gradient is present in the simulations, the acceleration parameter:

$$K = \frac{\nu}{u_e^2}\frac{du_e}{dx}, \tag{21}$$

is computed, where u_e is the boundary layer edge velocity. Substituting non-dimensional variables requires division by the Reynolds number associated with the governing equations to obtain the correct magnitude. Probing along the entire length of the domain, the acceleration parameter was found to be less than 3×10^{-8}. This is below the threshold where the mean flow becomes affected by a pressure gradient [30, 31] and supports the assumption that the pressure gradient is negligible in the present simulations.

5 Higher Reynolds Number Uncontrolled Simulations

With confidence that the flow solver is generating good results consistent with the approximation used, we seek to compare the implicit LES technique and the local ILSA subfilter model. We increase the momentum thickness Reynolds number to $Re_\theta = 3230$ in order to match experiments conducted at the University of Toronto [32, 33]. The smaller simulation domain is used for the comparison so that a larger set of simulation parameters can be considered. A coarser grid than at the lower Reynolds number is also used relative to turbulent scalings. This is especially true in the streamwise direction, which was thought to be the least important direction in flow. The results below show that the importance of the streamwise direction was under predicted.

A baseline turbulent flow field is generated for the comparative simulations using the medium grid described in Table 1. The solution is initialized with an empirical turbulent mean velocity profile and randomly perturbed. The solution is then advanced 1000 non-dimensional time units with a time step of $\Delta t = 0.1$. Separate simulations were run for the implicit LES technique and ILSA model. These baseline flow fields are then interpolated onto the appropriate grid using trilinear interpolation. The solution on each new grid is then advanced between 200 and 500 more time units to allow the flow to adjust to the new grid. It is these results which are presented in the discussion below.

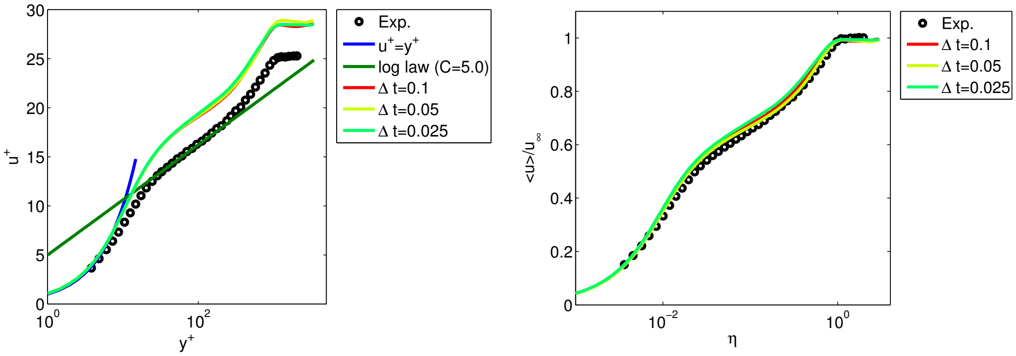

(a) Streamwise mean velocity profile.

(b) Streamwise mean velocity profile.

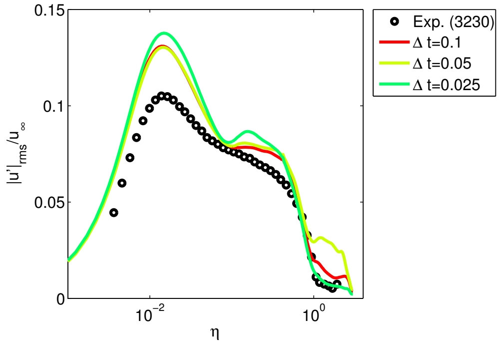

(c) Streamwise fluctuating velocity profile.

Figure 6: **Implicit LES - Temporal convergence at** $Re_\theta = 3230$

5.1 Implicit LES

General observations. As demonstrated in the previous section, the implicit LES technique performs reasonably well given that the subfilter modelling is not physically motivated. As expected, the quality of the results is highly dependent on the spatial grid used. This approach tends to be more robust than local ILSA model, though not always as consistent in the accuracy of the results.

Temporal resolution. In the same way that a coarse grid and artificial dissipation will damp high-frequency modes in the solution, so will a large time step with the L-stable ESDIRK4 time-marching method. Computationally we want to use as few time steps as possible to minimize time and resource costs, while retaining the important details of the flow. To evaluate this balance of computational cost and accuracy, we perform a temporal resolution study on the medium grid using three time step sizes: 0.1, 0.05, and 0.025.

Figures 6a and 6b compare the mean streamwise velocity profiles of the simulations, along with the empirical law of the wall and experimental measurements. Relative to the turbulent variables u^+ and y^+, the velocity is over predicted by a significant margin. This begins in the buffer layer and extends through the log region to the farfield. This is similar to what was observed at the lower Reynolds number, but to a greater extent. The slope in the log region is, however, reasonably well predicted. When compared relative to the freestream velocity, the mean velocity profile is in much better agreement. There is still some deviation in the buffer layer, but it is not nearly as significant and the computational results match well in the viscous sublayer and outer part of the boundary layer. With respect to temporal resolution, the figures show that the mean velocity profiles are not significantly affected by time step size. Some deviation is observed in the upper part of the log region, but the change is not monotonic relative to the step size.

The fluctuating velocity profile is shown in Figure 6c. In this case, we see that temporal resolution plays a significant role. Reducing the size of the time step increases the peak fluctuations in both the near wall and outer region of the boundary layer. This behaviour is likely correlated with the increased velocity observed mean velocity profile. The outer peak in the fluctuating velocity profile is not observed in the experiment

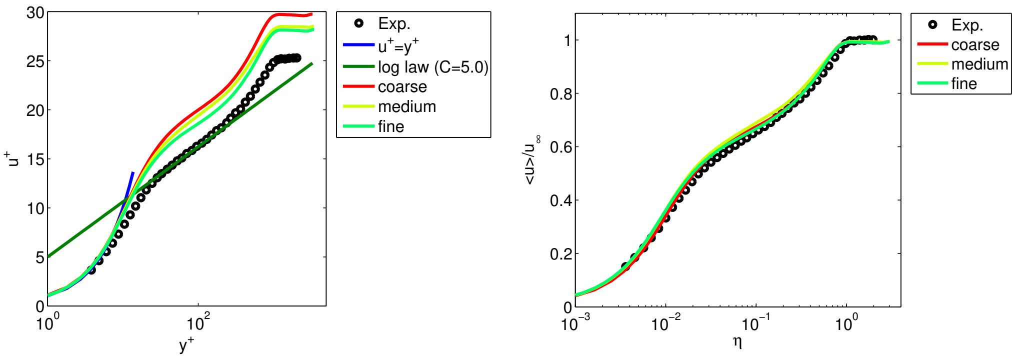

(a) Streamwise mean velocity profile.

(b) Streamwise mean velocity profile.

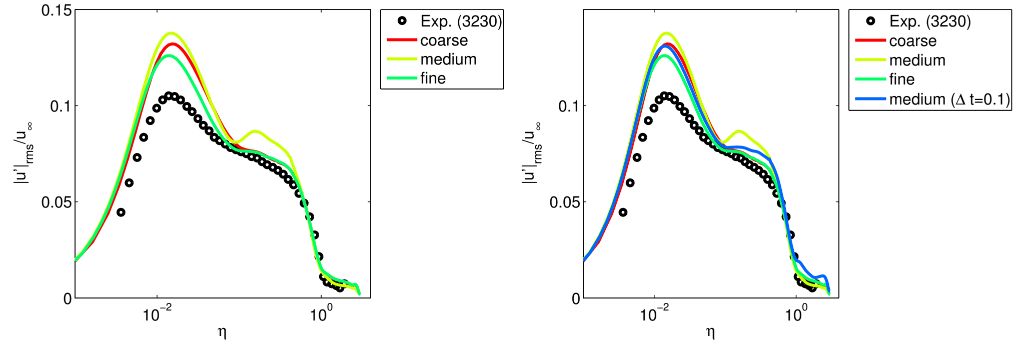

(c) Streamwise fluctuating velocity profile.

(d) Streamwise fluctuating velocity profile.

Figure 7: **Implicit LES - Spatial convergence at** $Re_\theta = 3230$

and must be taken as an error in the simulation. A potential source of this error is the use of a relatively small averaging time scale, which is discussed more below. If this is not the case, the plot indicates that there are larger sources of error in the simulations than the temporal resolution, which are highlighted as the step size is reduced. One area where the simulation match well the experiments, and the empirical result [34], is in the location of the near wall peak.

Throughout the range of time steps sizes evaluated, we found that the friction velocity Reynolds number Re_τ remains fairly constant. The average value of $Re_\tau = 1076$ is fairly close to the experimentally measured value of $Re_\tau = 1070$ at the target momentum thickness Reynolds number. The momentum thickness Reynolds number is also fairly constant across the range of time step sizes; however, it is larger than the target value. This may be due in part to the empirical relations used to set the simulation parameters, and due in part to LES modelling errors.

Spatial resolution. As expected, spatial resolution has a big impact on the implicit LES results. To demonstrate this, a spatial resolution study is carried out using three successively finer grids. These grids do not form a nested family of grids, in that the coarser grids are not obtained by removing every other node from the finer grids. Two considerations influenced this decision: 1) balancing the computational cost on the finest grid and the minimum resolution on the coarsest grid; and 2) having a similar off-wall spacing on the two finer grids. In this study a time step size of 0.025 is used.

As seen in Figure 7a the mean velocity in the buffer layer relative to the turbulent variables is much less over predicted as the mesh is refined. As before, this extends through log region and into the farfield. The improvement does not appear to be a function of the friction velocity, as it only varies by about 1% across the different grid levels. Less of a difference is observed relative to the mean velocity profile scaled by the freestream velocity shown in Figure 7b.

Considering the fluctuating velocity profile shown in Figure 7c, the fine grid is able to improve agreement in the near wall peak relative to the experimentally measured values. The result from the medium grid,

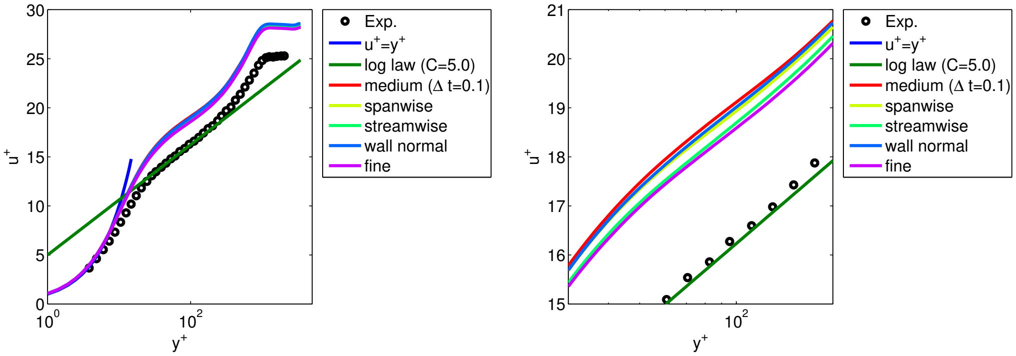

(a) Streamwise mean velocity profile. (b) Streamwise mean velocity profile.

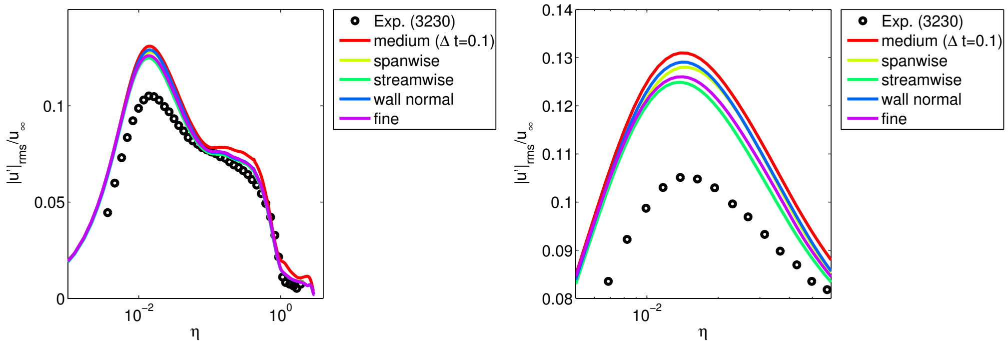

(c) Streamwise fluctuating velocity profile. (d) Streamwise fluctuating velocity profile.

Figure 8: **Implicit LES - Selective spatial refinement at** $Re_\theta = 3230$

however, appears to be an outlier using the time step size of $\Delta t = 0.25$. As mentioned previously, this is potentially due to the use of a small averaging time scale. A second profile for the medium grid obtained with a time step size of $\Delta t = 0.1$ is included in Figure 7d. This profile is more consistent the the expected result of sequential grid refinement, at least in the near wall peak.

The spatial refinement yields a small increase in friction velocity Reynolds number from 1049 on the coarse grid to 1128 on the fine grid. Nothing conclusive can be said about the change in momentum thickness Reynolds in this case, but it remains over predicted as in the temporal convergence study discussed above.

Selective spatial refinement. To explore the grid parameters that had the greatest impact on the solution, the medium grid is refined separately in the streamwise, spanwise, and wall normal directions. Our expectation was that either the spanwise or wall normal refinements would yield the greatest benefit. In the former case, this is based on the small spanwise scale of streamwise vortices near the wall, and in the latter case, on the fact that there are significant wall normal gradients near the wall. Surprisingly, the streamwise refinement yields the greatest improvement in the mean and fluctuating velocity profiles, as seen in Figures 8a through 8c. In fact, refining in the streamwise direction yields nearly the same results as the fine grid, which made use of refinement in all three directions. This result partially explains the change in quality of results between the lower Reynolds number simulations and the higher Reynolds number comparative studies. The former had spacing more than 3.5 times smaller in the streamwise direction.

Artificial dissipation. Extending the study of spatial resolution, we also consider the amount of artificial dissipation that is applied. Three values were considered for the fourth-dissipation coefficient: 0.05, 0.025, 0.0125. Halving the value once more led to an unstable simulation on the medium grid using a time step size of 0.025.

As with the grid density considered above, the lower values of the dissipation coefficient had an impact of the accuracy of the time-averaged values. Figure 9a shows improvements in the buffer and log layers of the

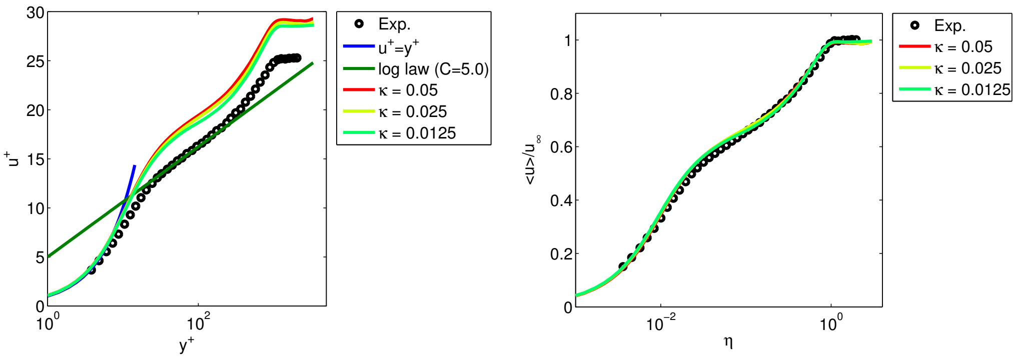

(a) Streamwise mean velocity profile.

(b) Streamwise mean velocity profile.

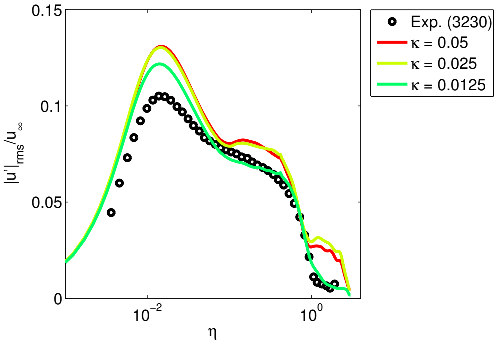

(c) Streamwise fluctuating velocity profile.

Figure 9: **Implicit LES - Artificial dissipation at** $Re_\theta = 3230$

mean velocity profile. The improvement is less significant than with the grid density, but is still noticeable. With the fluctuating velocity profile shown in Figure 9c, little difference is observed between the largest and middle values. The lowest value shows a significant improvement in the near wall peak, and the profile of the outer region is much smother. However, the outer region is somewhat under predicted.

In contrast to the spatial refinement, lowering the artificial dissipation coefficient also lowered the friction velocity Reynolds number. A similar trend was observed in the momentum thickness Reynolds number. Certainly a lower value of the dissipation coefficient is preferable, so long as the simulation remains stable.

Averaging time scale As seen in some of the results above, erroneous fluctuations are visible in the outer part of the boundary layer, and even in the farfield. To evaluate the source of this error, a number of simulation parameters were varied one by one to evaluate which had the greatest influence in the farfield. The parameters included in the study were: the type of boundary conditions, the type of block interface SAT, the order of the dissipation model used, the averaging time scale used for the turbulent inflow and convective outflow boundary conditions, and a modification of the inflow boundary to enforce a laminar freestream $2.5\delta_\circ$ above the wall. This parameter study was carried out using the coarse grid and a relatively large time step of 0.05. The results (not shown here) indicated that increasing the averaging time scale had the most positive impact in the farfield. By increasing the averaging time scale from 8 to 40 nearly eliminated all the farfield fluctuations.

5.2 Local ILSA subfilter model

For the local ILSA simulations presented below, we use a subfilter activity level of $s_\tau = 0.02$ and a model averaging time scale of 1 non-dimensional time unit, unless specified otherwise. This was done to test the model's suitability for application to the controlled case, where the mean flow is time dependant. The results are compared to a longer averaging time below.

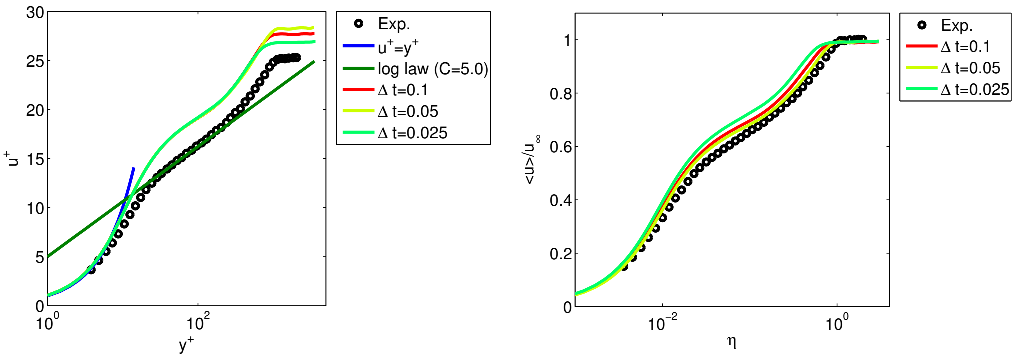

(a) Streamwise mean velocity profile.

(b) Streamwise mean velocity profile.

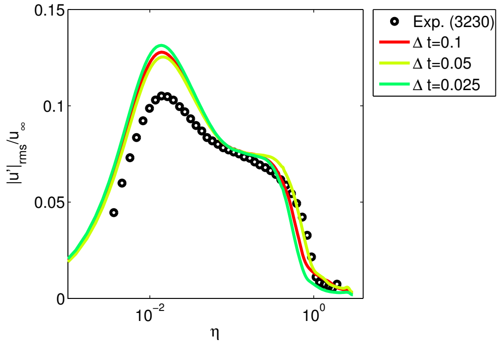

(c) Streamwise fluctuating velocity profile.

Figure 10: **Local ILSA - Temporal convergence at $Re_\theta = 3230$:**

General observations. In general, we found that the local ILSA model performs well compared to the implicit LES approach. The results obtained from the local ILSA model tend to be more consistent and accurate when using the same simulation parameters. While the model requires the computation of a turbulent eddy viscosity, we found that the local ILSA model required less CPU time per time step than the implicit LES approach. This largely comes from a $15 - 20\%$ reduction in linear iterations. However, in order to checkpoint and restart the simulations requires significantly more information to be written to disk. Specifically, this includes all the averaged nodal quantities required by the model $(< u_i >, < S_{i,j} >, < \mathcal{K} >, < \epsilon >, < \chi_i >)$. While the results generated from the local ILSA model are more consistent and the solution times lower, the use of the model was found to be less robust. In early stages of a simulation, while the flow is still developing, instabilities sometimes stopped the solution. Once the flow was developed, the boundary layer thickness would occasionally blow up. Recovery from both failures was possible by backtracking and adjusting the simulation parameters slightly.

Temporal resolution. The temporal resolution study presented for the implicit LES technique is repeated here for the ILSA model. This was done with the same grid, time step size, and general simulation parameters, but using a baseline flow field generated with the ILSA model.

The mean velocity profiles computed relative to turbulent variables are shown in Figure 10a. The general qualities are similar to the implicit LES approach. This includes the agreement in the viscous sublayer and the magnitude of the overshoot in the buffer layer, which then extends through the log region to the farfield. As with the implicit LES techniques, little variation is seen as the time step is changed. In the case of the ILSA model, this even less in the log region than the implicit LES approach.

In contrast, there is more variation in the mean velocity profile when scaled by the freestream velocity. It may be that the boundary layer thickness is being over prediction in this case. As mentioned previously, the boundary layer thickness has diverged on occasion when using the ILSA model. As with the implicit LES simulations, the disagreement is most significant with the finest time step size. A similar disagreement

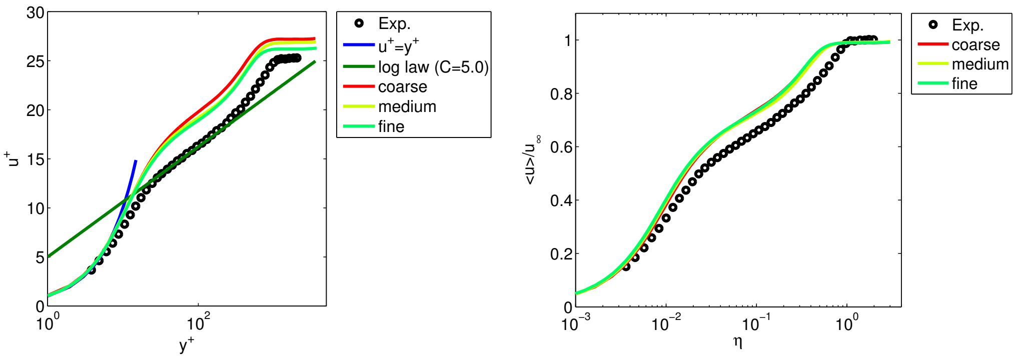

(a) Streamwise mean velocity profile.

(b) Streamwise mean velocity profile.

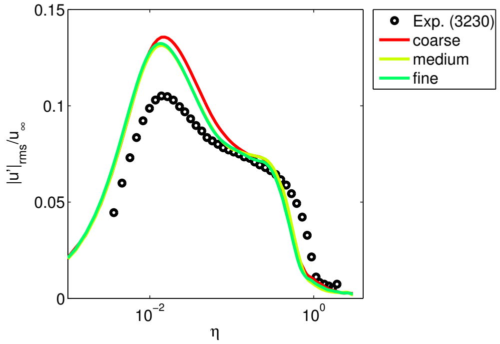

(c) Streamwise fluctuating velocity profile.

Figure 11: **Local ILSA - Spatial convergence at $Re_\theta = 3230$:**

is also observed in the fluctuating velocity profile shown in Figure 10c, where it appears the simulations have slightly different boundary layer thicknesses. In general, agreement is slightly better in the near wall peak region as compared with implicit LES approach, and the results are significantly improved in the outer layer.

As with the implicit LES simulation, little variation in the friction velocity Reynolds number is observed. In contrast, the momentum thickness Reynolds number improves dramatically with the finest time step size. This was also observed in other local ILSA simulations using the smaller step size. Future work should investigate the potential trade-offs of using even smaller step sizes.

Spatial resolution. Spatial resolution is expected to influence the ILSA simulations differently than those using the implicit LES technique. This is due to the grid independent construction of the ILSA model and the use of a prescribed level of subfilter activity. Indeed this behaviour is visible in the spatial resolution study which we carry out. The results of this study are shown in Figures 11a through 11c. A noticeable improvement is observed between the coarse and medium grid, but almost none between the medium and fine grid. A consequence of this behaviour, for the grids tested, is that the implicit LES generates a more accurate solution to the mean velocity profile on the fine grid than the ILSA model. However, the ILSA model does produce a more accurate profile of the fluctuating velocity.

In this case, both the friction velocity and momentum thickness Reynolds numbers only change slightly with grid resolution.

Artificial dissipation. As the local ILSA model introduces additional dissipation through the turbulent eddy viscosity, it is interesting to see how the amount of artificial dissipation influences the results. In general, it has been observed that less artificial dissipation is needed when using the ILSA model, than when using the implicit LES technique. Therefore, we consider three values of the fourth-dissipation coefficient, which are half as large as used with the implicit LES technique: 0.025, 0.0125, and 0.00625. Halving the dissipation coefficient again, on the medium grid with time step of 0.025, led to an unstable simulation.

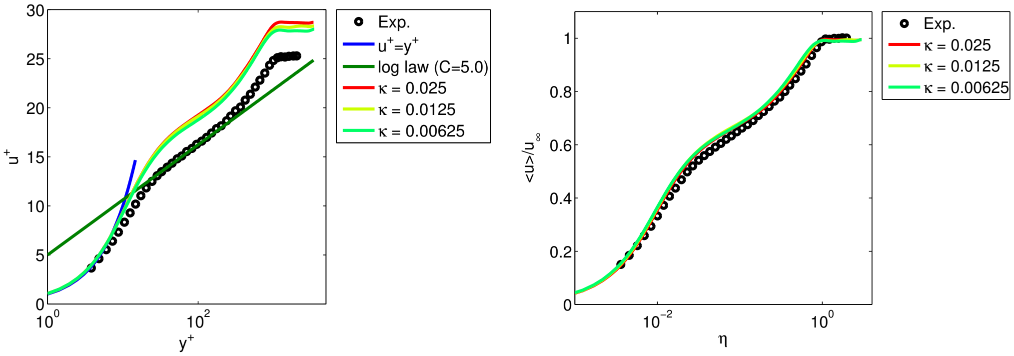

(a) Streamwise mean velocity profile.

(b) Streamwise mean velocity profile.

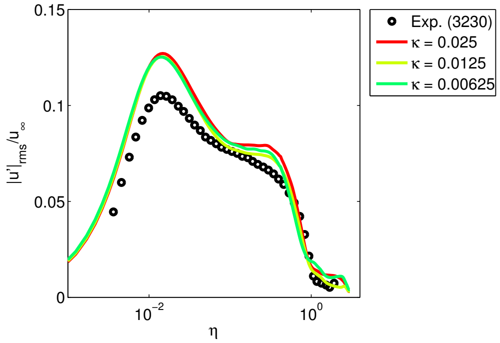

(c) Streamwise fluctuating velocity profile.

Figure 12: **Local ILSA - Artificial dissipation at** $Re_\theta = 3230$**:**

The results of this test are shown in Figures 12a through 12c. As with the temporal refinement study, the ILSA model did not appear to be very sensitive to the value of the dissipation coefficient. Small improvements in the mean velocity profile are observed, but less significantly than with the implicit LES approach. In the case of the fluctuating velocity profile, there is minimal improvement in the near wall peak, and the intermediate value yields a slightly better result in the outer part of the boundary layer.

In contrast to the results obtained with the implicit LES approach, the friction velocity Reynolds number increases slightly as the dissipation coefficient is lowered. However, both approach the experimentally measured value: implicit LES from above and local ILSA from below.

Averaging time scale. The ILSA simulations suffer less from erroneous fluctuations in the farfield; however, the same parameter study done for the implicit LES approach is repeated here. As before, the most significant impact on the results comes from increasing the averaging time scale used for the turbulent inflow and convective outflow boundary conditions.

Local ILSA subfilter model averaging time scale. Simulations using the ILSA model have a second averaging parameter, for the quantities in the ILSA model itself. For this study we have been using time as the homogeneous direction in the flow. As with the inflow and outflow boundaries, one would expect that increasing the averaging time scale would be beneficial. The challenge comes when we want to consider control using synthetic jets. In this case, the mean flow near the jet and downstream from the jet is not steady. Therefore, controlled simulations using the ILSA model need to balance averaging out the turbulence, and capturing the time dependent nature of the mean flow.

To evaluate the model's response to the averaging time scale, we considered two simulations with time scales of 1 and 40. Results (not shown here) yield almost no difference in the mean velocity profile. The longer averaging time scale did improve the agreement in the outer boundary layer slightly, but little difference is observed in the near wall peak.

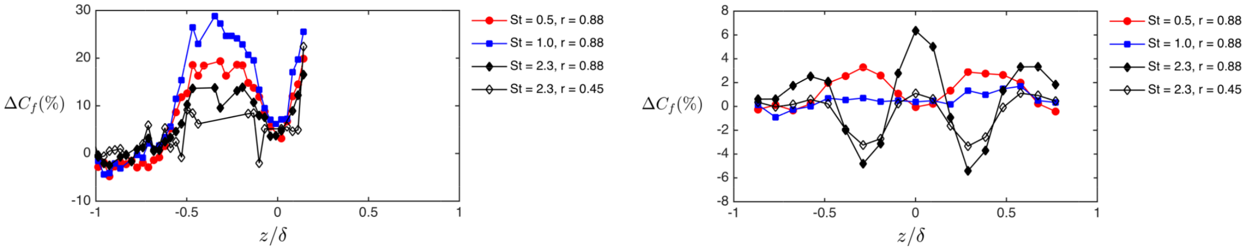

11.5 x/δ

15 x/δ

Figure 13: **Experimental - St=2.3, r=0.44:** Change in skin friction coefficient evaluated using oil film interferometry for a single jet $z/\delta = [0.15, 0.45]$ [left] and the Clauser chart method from hot-wire data for two jets $z/\delta = [0.15, 0.45]$ and $[-0.15, -0.45]$ [right]. Jet are located at $10\delta_\circ$.

6 Controlled Simulations

In this section we evaluate the two LES approaches for simulating flow control using a single spanwise oriented synthetic jet. In this case, we chose a slightly higher momentum thickness Reynolds number of 4210. The jet used in these simulations has a spanwise size of $0.3\delta_\circ$ and an aspect ratio of 13 : 1. This simulation condition and jet geometry are chosen to match the experimental setup at the University of Toronto [32, 33]. The Mach number remains at 0.2 and the time step Δt is chosen to be 1/10th of the jet cycle period, ~ 0.217. The averaging time scale used in these simulations was 20 non-dimensional time units.

We define the jet actuation with two parameters: the Strouhal number $St = \delta f/u_\infty$ and blowing ratio $r = u_{\text{jet}}/u_\infty$, where δ is the boundary layer thickness, f is the forcing frequency, u_{jet} is half of the average jet exit velocity over the blowing cycle, and u_∞ is the freestream flow velocity. Experimental results identified the jet parameters of Strouhal number 2.3 and blowing ratio 0.44 as potentially leading to a reduction in skin friction drag. This was based on hot-wire and oil-film interferometry located 1.5 and 5 $\delta_\circ$ downstream of the jet, respectively, shown in Figure 13. The potential for drag reduction motivated the numerical investigation of these jet parameters. However, subsequent experimental measurements made with hot films at a greater number of measurement locations indicate the reverse to be true. It appears that there are pockets of reduced skin friction, but the overall influence of the jet will lead to an increase in skin friction drag.

6.1 Implicit LES technique

General observations. The introduction of flow control using a synthetic jet adds extra challenges for the numerical simulation. To avoid instabilities requires much greater care in the selection of simulation parameters. Much of the instability comes from within the slot of the jet. Occasionally, instabilities also manifest just above the jet exit. In order to alleviate the step size restriction these instabilities create, the fourth-difference dissipation coefficient is set to the largest value considered in the uncontrolled simulations of 0.05. Furthermore, second-difference dissipation is added within the slot itself. Second-difference dissipation reduces the spatial order to unity and is almost exclusively reserved for dealing with shocks. However, given that we are not that interested in this study with the flow inside the jet (we are already modelling the diaphragm and cavity), we found this to be a reasonable compromise to accelerate the simulations.

Change in skin friction Figure 14 shows the map of the change in time-averaged skin friction coefficient resulting from the synthetic jet actuation. It shows an elongated strip of skin friction reduction both upstream and downstream of the jet along its centerline. The maps of the change in phase-averaged skin friction shown in Figure 15 provide further insight. These show that the long region of reduced skin friction drag downstream of the jet persists throughout the entire cycle. The region of reduced skin friction upstream of the jet grows from the end of the blowing phase through to the mid point in the suction phase before decaying again.

Two long regions of increased skin friction drag emanate from the edges of the jet, and a third shorter region forms downstream along the jet's centerline. Integrating the skin friction over the region spanned by $\{x \times z\} = \{[5, 15] \times [0, 3]\}\delta_\circ$, excluding the spanwise strip where the jet is located $x = [9.99, 10.01]\delta_\circ$, yields

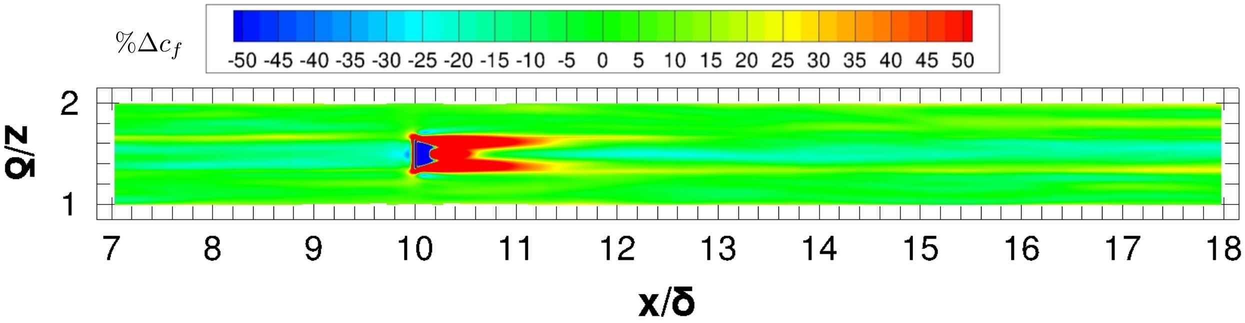

Figure 14: **Implicit LES - St=2.3, r=0.44:** Spatial map of change in time-averaged skin friction coefficient resulting from synthetic jet actuation.

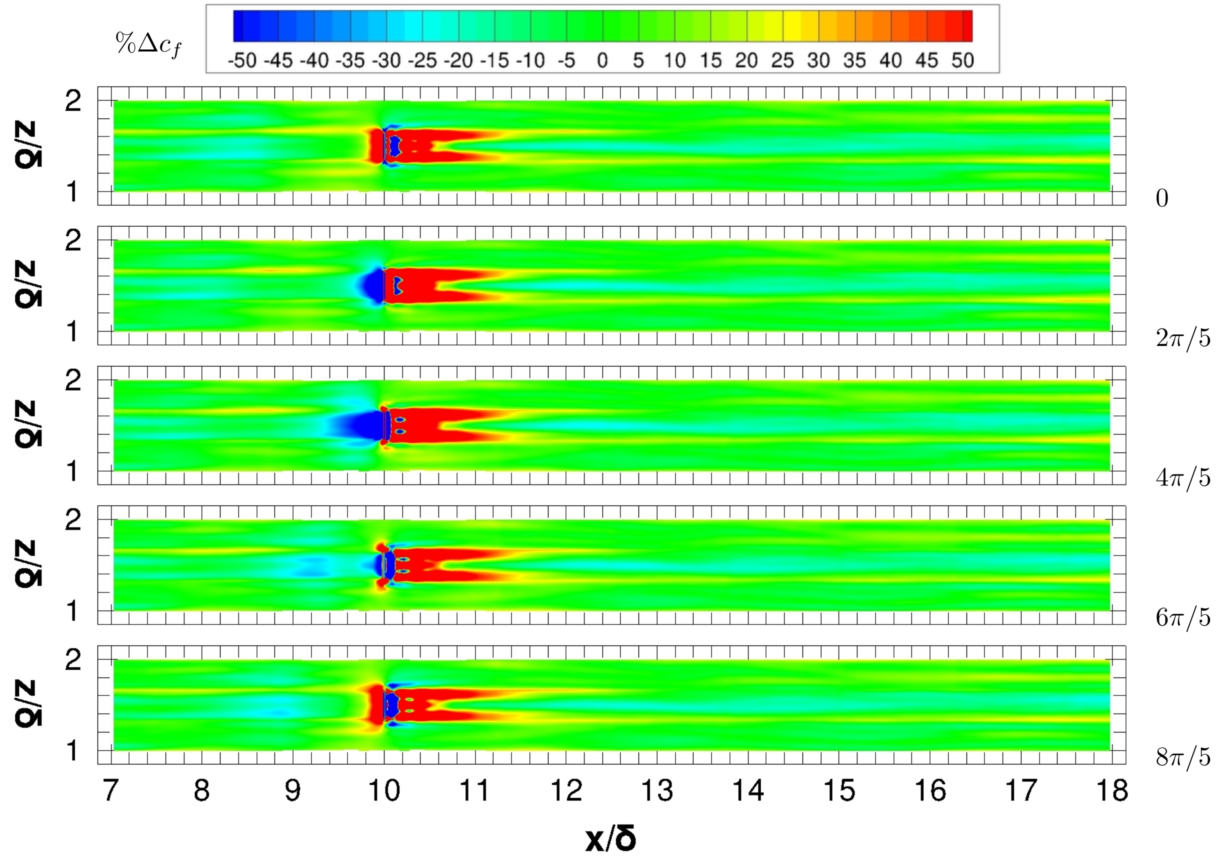

Figure 15: **Implicit LES - St=2.3, r=0.44:** Spatial maps of change in phase-averaged skin friction coefficient.

an increase in drag of about 1.7%. Despite the large increase in drag near the jet, the long strips of drag reduction along the jet's centerline minimize the impact on the overall result. Future work should investigate small variations on these parameters to see if the persistent region of drag reduction can be maintained while minimizing the increase in drag right at the jet. It may also be worth introducing some type of feed-forward controller to better target specific structures in the flow.

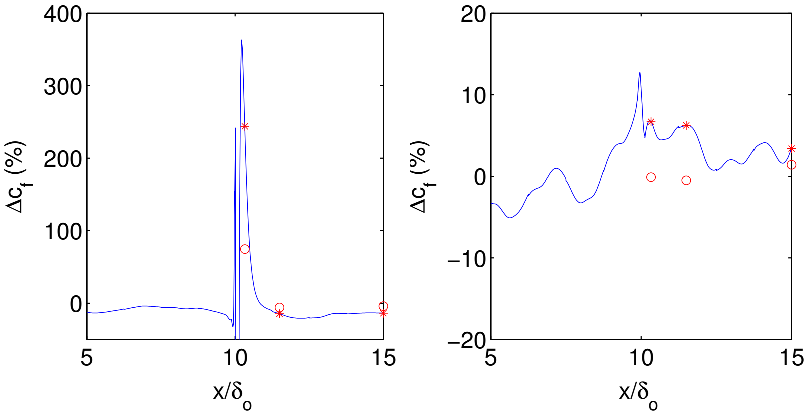

Figure 16: **St=2.3, r=0.44:** Change in time-averaged skin friction coefficient along jet centerline [left] and along the streamwise line between the jets [right]. Open symbols are from the experimental data; asterisks are the same points from the computations.

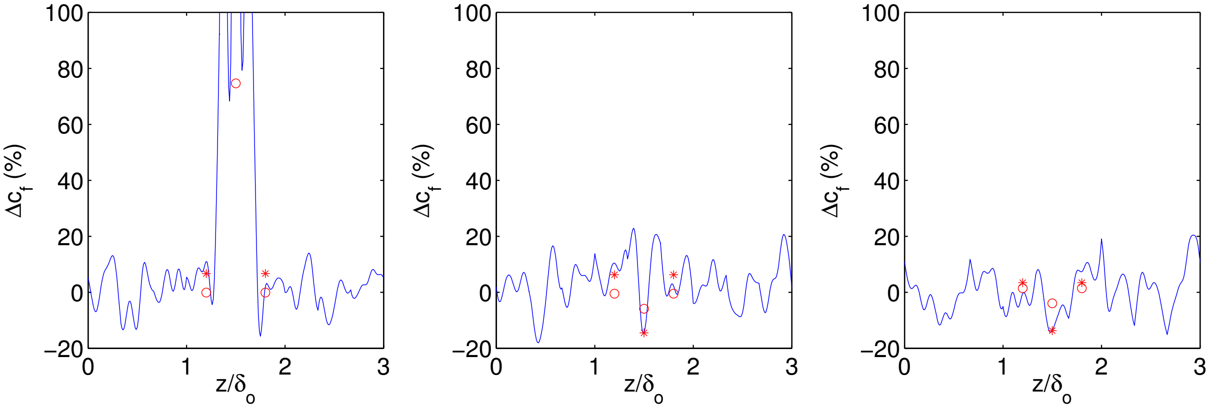

Figure 17: **St=2.3, r=0.44:** Change in time-averaged skin friction coefficient along spanwise lines of $x = 10.33\delta_\circ$ [left], $x = 11.5\delta_\circ$ [middle], and $x = 15\delta_\circ$ [right]. Open symbols are from the experimental data; asterisks are the same points from the simulations. The lines are also from simulation data.

6.1.1 Comparison with experiment

Figures 16 and 17 compare the change in time-averaged skin friction coefficient along the streamwise and spanwise lines corresponding to experimental hot film measurement locations. Note that the off-center experimental values highlighted are repeated values. Measurements were only taken to one side of the jet, not both. The off-center numerical results highlighted are averaged values from both sides of the jet. Strong gradients are visible around some of the measurement locations, both in the streamwise and spanwise direction. Thus small inaccuracies in sensor placement or variations in the flow direction in the experiments could have a significant impact on the results. Furthermore the figures indicate that further time-averaging would benefit the computational results. Considering the figures together, the numerical results show reasonably good agreement with the experimental measurements.

6.2 Local ILSA subfilter model

Several attempts were made to apply the ILSA model to the controlled simulations described above. However, using the same grid and similar simulation parameters, the initial step size required to maintain stability with the ILSA model is more than two orders of magnitude smaller than with the implicit LES technique. This can be gradually increased, but must remain about an order of magnitude smaller once the simulation settles down. For long time simulations this is very costly; therefore, no controlled simulation results are presented for the ILSA model. Similar to the implicit LES technique, the instability in the simulations originates in the synthetic jet slot or just above the slot. Adding second-dissipation within the slot did not stabilize the simulation. The only means we found to increase the time step size further, was to sacrifice the depth of convergence of the residual on each time step from $< 10^{-8}$ to $< 10^{-4}$. This is not ideal.

7 Conclusions

This paper compares two large-eddy simulation techniques for the simulation of turbulent boundary layers and flow control using synthetic jets. The first approach is the implicit LES technique. In this case we solve the Navier-Stokes equations and unresolved modes are damped by fourth-difference matrix artificial dissipation compatible with the summation-by-parts spatial discretization. The second technique considered is the local ILSA subfilter LES model. It solves the Favre-filtered Navier-Stokes equations with an algebraic eddy-viscosity model for the unresolved modes. The model uses mesh-independent approximation of the integral length scale and prescribes a certain level of subfilter turbulent activity locally through a spatially and temporally varying model coefficient.

The implicit LES approach requires no additional equations to be solved; therefore it is relatively efficient. It is also found to be very robust. An initial low Reynolds number simulation using the implicit LES technique verifies the flow solver for solving zero pressure gradient flat plate boundary layers. Analysis shows very little influence from compressibility effects or erroneous pressure gradients.

In the comparative studies, the temporal resolution did not have the expected impact on the quality of the implicit LES results. Increasing the temporal resolution did not improve agreement in the buffer layer, rather it highlighted erroneous fluctuations in the outer part of the boundary layer. Additional simulations found that increasing the averaging time scale used in the turbulent inflow and convective outflow boundary conditions minimizes erroneous fluctuations in the farfield which might be corrupting these conclusions. In contrast, spatial resolution did have the expected influence on the results. However, it was the streamwise resolution, rather than spanwise or wall normal resolution, that had the most beneficial effect on the results. The studies also showed that minimizing artificial dissipation can have a small but beneficial impact on the quality of the results.

The local ILSA model performed very well. Despite requiring the evaluation of an additional algebraic equation, the solution time was reduced relative to implicit LES. This came from a $15 - 20\%$ reduction in linear iterations. The ILSA model also produced more consistent and accurate results. However, the model was found to be less robust. In the comparative studies, the temporal resolution had little effect on the velocity profiles, but the finest time step considered did improve the agreement in momentum thickness Reynolds number. Spatial convergence studies highlighted the grid-independent nature of the model, but also prevented further improvements on the finest grid. The additional dissipation from the ILSA model enabled lower values of artificial dissipation to be used. However, little change is observed in the results as the dissipation coefficient is changed. Larger averaging time scales for the model variables generated slightly better results; however, the shorter time scale used in the majority of the simulations did not affect the results greatly.

For the controlled simulations, only the implicit LES approach was able to consistently generate results. This was aided by a slight increase in fourth-difference dissipation and the addition of second-difference dissispation within the slot only. The results generated by the implicit LES approach are in reasonably good agreement with experiment. They also give much more detail of the spatial change in time-averaged skin friction. In contrast, the local ILSA model required a time step one to two orders of magnitude smaller than the implicit LES technique in order to maintain stability of the simulation, even with additional dissipation.

In summary, the local ILSA model provides many benefits relative to the implicit LES technique for uncontrolled turbulent boundary layers. More work is needed to apply the model to the controlled case. The implicit LES approach is less consistent in the quality of results but more robust.

References

[1] IATA. IATA Economics Briefing: Airline Fuel and Labour Cost Share. Febuary 2010.
[2] ATAG. Aviation: Benefits Beyond Borders. Technical report, April 2014.

[3] ATAG. Beginner's Guide to Aviation Efficiency. Technical report, Nov 2010.

[4] T. Tyler. IATA Annual Review 2014. Technical report, June 2014.

[5] N. Hutchins and I. Marusic. Evidence of very long meandering features in the logarithmic region of turbulent boundary layers. *Journal of Fluid Mechanics*, 579:1–28, 2007.

[6] N. Hutchins and I. Marusic. Large-scale influences in near-wall turbulence. *Royal Society of London Philosophical Transactions Series A*, 365:647–664, 2007.

[7] M. Galbraith and M. Visbal. Implicit large eddy simulation of low reynolds number flow past the sd7003 airfoil. *46th AIAA Aerospace Sciences Meeting and Exhibit*, AIAA-2008-225, 2008.

[8] K. Ritos, I. W. Kokkinakis, D. Drikakis, and S. M. Spottswood. Implicit large eddy simulation of acoustic loading in supersonic turbulent boundary layers. *Physics of Fluids*, 29:046101, 2017.

[9] S. Sekhar and N. Mansour. Implicit large-eddy simulations of zero-pressure gradient, turbulent boundary layer. *53rd AIAA Aerospace Sciences Meeting*, AIAA-2015-1987, 2015.

[10] A. Rouhi, U. Piomelli, and B. J. Geurts. Dynamic subfilter-scale stress model for large-eddy simulations. *Physical Review Fluids*, 1(4):044401, 2016.

[11] C. A. Kennedy and M. H. Carpenter. Additive Runge-Kutta Schemes for Convection-Diffusion-Reaction Equations. *Applied Numerical Mathematics*, 44(1-2):139–181, January 2003.

[12] P. D. Boom and D. W. Zingg. Time-Accurate Flow Simulations Using an Efficient Newton-Krylov-Schur Approach with High-Order Temporal and Spatial Discretization. *51st AIAA Aerospace Sciences Meeting*, AIAA-2013-0383, 2013.

[13] D. C. Del Rey Fernández and D. W. Zingg. High-order compact-stencil summation-by-parts operators for the second derivative with variable coefficients. *ICCFD7-2803*, 2012.

[14] J. E. Hicken and D. W. Zingg. A parallel Newton-Krylov solver for the Euler equations discretized using simultaneous approximation terms. *AIAA Journal*, 46(11):2773–2786, 2008.

[15] M. Osusky, P. Boom, D. Del Rey Fernández, and D. Zingg. An efficient newton-krylov-schur parallel solution algorithm for the steady and unsteady navier-stokes equations. *ICCFD7-1801*, 2012.

[16] M. Osusky and D. W. Zingg. Parallel Newton-Krylov-Schur Solver for the Navier-Stokes Equations Discretized Using Summation-By-Parts Operators. *AIAA Journal*, 51(12):2833–2851, dec 2013.

[17] T. S. Lund, X. Wu, and K. D. Squires. Generation of turbulent inflow data for spatially-developing boundary layer simulations. 140:233–258, 1998.

[18] S. Stolz and N. A. Adams. Les of supersonic boundary layers using the approximate deconvolution model. *Direct and Large-Eddy Simulation – IV*, pages 269–276, 2001.

[19] J. H. Ferziger and M. Peric. *Computational Methods for Fluid Dynamics*. Springer, 2002.

[20] T. Sayadi and P. Moin. Predicting natural transition using large eddy simulation. *Center for Turbulence Research Annual Research Briefs*, pages 97–108, 2011.

[21] P. Schlatter. *Large-eddy simulation of transition and turbulence in wall-bounded shear flow*. PhD thesis, Swiss Federal Institute of Technology, 2005.

[22] P. Sagaut, E. Garnier, E. Tromeur, L. Larchevêque, and E. Labourasse. Turbulent inflow conditions for large-eddy simulation of compressible wall-bounded flows. *AIAA Journal*, 42(3):469–477, 2004.

[23] X. Wu and P. Moin. Direct numerical simulation of turbulence in a nominally zero-pressure-gradient flat-plate boundary layer. *Journal of Fluid Mechanics*, 630:5–41, 2009.

[24] Alfredsson, P.H., Örlü, R. and Segalini, A. A new formulation for the streamwise turbulence intensity distribution in wall-bounded turbulent flows. *European Journal of Mechanics – B/Fluids*, 36:167–175, 2012.

[25] Alfredsson, P. H., Örlü, R., Kurian, T., Fransson, J. H. M., Segalini, A. and Rüedi, J. -D. and Talamelli, A. The diagnostic plot – a new way to appraise turbulent boundary-layer data. *Advances in Turbulence XII*, 132:609–612, 2009.

[26] T. Cebeci. *Analysis of Turbulent Flows with Computer Programs*. Elsevier, 2013.

[27] L. Wei. *Direct Numerical Simulation of Compressible and Incompressible Wall Bounded Turbulent Flows with Pressure Gradients*. PhD thesis, Queen's University, 2009.

[28] O. Cabrit and F. Nicoud. Direct simulations for wall modeling of multicomponent reacting compressible turbulent flows. *Physics of Fluids*, 21(5):055108, 2009.

[29] E. R. V. Driest. Turbulent Boundary Layer in Compressible Fluids. *Journal of the Aeronautical Sciences*, 18(3):145–160, 1951.

[30] M. Schultz and K. A. Flack. Turbulent boundary layers on a systematically varied rough wall. *Physics*

of Fluids, 21:015104, 2009.

[31] V. Patel. Calibration of the preston tube and limitations on its use in pressure gradients. *Journal of Fluid Mechanics*, 23(1):185–208, 1965.

[32] R. E. Hanson, B. Ganapathisubramani, P. Lavoie, and T. Berk. Temporal and spatial response of a turbulent boundary layer to forcing by synthetic jets. *69th Annual Meeting of the APS Division of Fluid Dynamics*, 61(20):http://meetings.aps.org/link/BAPS.2016.DFD.R32.4, 2016.

[33] R. Belanger, P. D. Boom, R. E. Hanson, and D. W. Zingg. Skin friction drag reduction on a flat plate turbulent boundary layer using synthetic jets. *70th Annual Meeting of the APS Division of Fluid Dynamics* , 62(14):http://meetings.aps.org/link/BAPS.2017.DFD.F16.3, 2017.

[34] N. Hutchins, T. B. Nickels, I. Marusic, and M. S. Chong. Hot-wire spatial resolution issues in wall-bounded turbulence. *Journal of Fluid Mechanics*, 635:103, 2009.